JOURNAL OF GEOPHYSICAL RESEARCH, VOL. ???, XXXX, DOI:10.1029/,

Compaction around a rigid, circular inclusion in partially molten rock

Laura Alisic[1], John F. Rudge[1], Richard F. Katz[2], Garth N. Wells[3], and Sander Rhebergen[2,4]

Corresponding author: Laura Alisic, Bullard Laboratories, Department of Earth Sciences, University of Cambridge, Madingley Road, Cambridge, CB3 0EZ, United Kingdom (la339@cam.ac.uk)

[1]Bullard Laboratories, Department of Earth Sciences, University of Cambridge, United Kingdom.

[2]Department of Earth Sciences, University of Oxford, United Kingdom.

[3]Department of Engineering, University of Cambridge, United Kingdom.

[4]Mathematical Institute, University of Oxford, United Kingdom.

Abstract. Conservation laws that describe the behavior of partially molten mantle rock have been established for several decades, but the associated rheology remains poorly understood. Constraints on the rheology may be obtained from recently published experiments involving deformation of partially molten rock around a rigid, spherical inclusion. These experiments give rise to patterns of melt segregation that exhibit the competing effects of pressure shadows and melt-rich bands. Such patterns provide an opportunity to infer rheological parameters through comparison with models based on the conservation laws and constitutive relations that hypothetically govern the system. To this end, we have developed software tools to simulate finite strain, two-phase flow around a circular inclusion in a configuration that mirrors the experiments. Simulations indicate that the evolution of porosity is predominantly controlled by the porosity-weakening exponent of the shear viscosity and the poorly known bulk viscosity. In two-dimensional simulations presented here, we find that the balance of pressure shadows and melt-rich bands observed in experiments only occurs for bulk-to-shear-viscosity ratio of less than about five. However, the evolution of porosity in simulations with such low bulk viscosity exceeds physical bounds at unrealistically small strain due to the unchecked, exponential growth of the porosity variations. Processes that limit or balance porosity localization should be incorporated in the formulation of the model to produce results that are consistent with the porosity evolution in experiments.

1. Introduction

Segregation and extraction of melt from the mantle control the chemical evolution of the mantle and crust over geological time. Observations of petrological and isotopic disequilibrium suggest that melt extraction to produce oceanic crust is rapid and potentially localized into channels [*Kelemen et al.*, 1997]. The mechanics of such melt extraction processes are still somewhat mysterious. Equations that are thought to describe melt extraction are well established [*McKenzie*, 1984], but these require refinement and validation. In particular, although the relevant conservation principles are known, the constitutive laws and closure conditions remain poorly constrained.

New experiments by *Qi et al.* [2013] provide an opportunity to improve our understanding of the rheology of partially molten rocks. In these experiments, a fine-grained, partially molten aggregate of olivine and basalt is deformed around a nearly rigid, olivine sphere. The experimental samples start with an approximately uniform porosity; after they are deformed, quenched, and sectioned to reveal the resulting distribution of olivine and basaltic melt, they show clear evidence for melt migration within the sample. Measurements of the resulting patterns show that the spherical inclusion induces a perturbation to the pressure field around it, driving flow of magma from the high-pressure sectors to the low-pressure sectors. These sectors are known as pressure shadows.

Experimental results from a subset of the experiments by *Qi et al.* [2013] indicate that the pressure shadows can interact with emergent bands of high melt fraction. These bands are the result of a known instability in deforming, partially molten aggregates. This instability has been investigated theoretically [*Stevenson*, 1989; *Spiegelman*, 2003;

Katz et al., 2006; *Butler*, 2009, 2010; *Takei and Katz*, 2013; *Katz and Takei*, 2013] and experimentally [*Holtzman et al.*, 2003; *King et al.*, 2010] and has been shown to produce melt-enriched bands at a low angle to the shear plane. In the experiments by *Qi et al.* [2013], such melt bands nucleate at or near the pressure shadows, and grow at the expense of the shadows.

The present work aims to derive constraints on the rheology of the partially molten mantle from the aforementioned experiments. We hypothesize that the theory developed to model partially molten aggregates [*McKenzie*, 1984] can be used to describe the results obtained by *Qi et al.* [2013] if the correct constitutive laws are included. In particular, we seek to quantify the form and magnitude of the viscous resistance to compaction based on comparisons between numerical simulations, analytical solutions, and laboratory experiments. Moreover, our goal is to establish a framework for the interpretation of current and future laboratory experiments that is based on the two-phase dynamics of partially molten aggregates.

Previous analysis by *McKenzie and Holness* [2000] modeled melt segregation into pressure shadows around a rigid inclusion based on the theory of *McKenzie* [1984]. The authors show that the pattern of compaction and decompaction is sensitive to the ratio of the bulk to shear viscosity. They develop analytical solutions for an extremal case where the compaction length, the intrinsic length scale associated with the two-phase dynamics, is much larger than the size of the rigid inclusion, and is hence approximated as being infinite. And in this context, they solved only for the instantaneous pattern of pressure and (de)compaction associated with the onset of flow. In contrast with this analysis, experiments are performed with a compaction length that is on the order of the size of the spherical inclusion. Furthermore, patterns in experiments develop over finite strain, during which segregation of melt and solid modifies the viscosity structure, and the inclusion undergoes finite rotation. This is further complicated by the emergence of melt bands in the experiments, and hence there is an interaction and competition between the two modes of melt segregation. Hence the models of *McKenzie and Holness* [2000], while instructive, cannot be used to quantify constitutive parameters. The present work addresses these deficiencies by computing time-dependent solutions of the governing equations for a partially molten aggregate with finite compaction length.

We use a finite element discretization and implement the simulation code in the FEniCS software framework [*Logg et al.*, 2012; *Logg and Wells*, 2010]. FEniCS is an advanced library of tools for finite element modeling. Our numerical solutions extend a new set of analytical solutions for the instantaneous compaction rate surrounding a spherical inclusion at arbitrary compaction length [*Rudge*, 2013]. The simulation code is benchmarked against analytical theory, and our results are compared with patterns observed in experiments by *Qi et al.* [2013].

The manuscript is organized as follows. We first describe the governing equations of two-phase mantle flow and discuss the numerical methods used to model them. Next, a pair of benchmarks is presented: the first tests our calculation of instantaneous compaction around a circular inclusion; the second examines the growth rate and advection of porosity bands. We then explore the role of rheological parameters in three different model configurations of increasing complexity. The first suite of simulations addresses the formation of melt bands in a medium with randomly distributed melt, but without a rigid inclusion. The second suite focuses on the evolution of pressure shadows around a circular inclusion for an initially uniform porosity field. The final set of simulations incorporates both the random initial porosity and the rigid, circular inclusion. We examine the competition between melt bands and pressure shadows, and compare these simulations with previous experimental results.

2. Governing Equations

Mass and linear momentum balances for a two-phase (partially molten) system in a domain $\Omega \subset \mathbb{R}^d$, $1 \leq d \leq 3$, can be written as follows [*McKenzie*, 1984]:

$$\frac{\partial \phi}{\partial t} + \nabla \cdot (1 - \phi)\, \mathbf{u}_s = 0\,, \tag{1}$$

$$\nabla \cdot \bar{\mathbf{u}} = 0\,, \tag{2}$$

$$\phi(\mathbf{u}_f - \mathbf{u}_s) = -\frac{K_\phi}{\mu_f} \nabla p_f, \tag{3}$$

$$\nabla \cdot \bar{\boldsymbol{\sigma}} = \mathbf{0}\,, \tag{4}$$

where ϕ is the porosity, $\mathbf{u}_s$ is the solid velocity, $\mathbf{u}_f$ is the fluid velocity, and $\bar{\mathbf{u}} = \phi \mathbf{u}_f + (1 - \phi)\mathbf{u}_s$. The fluid pressure is given by p_f; μ_f is the fluid viscosity. K_ϕ is the permeability, with the subscript ϕ denoting a dependence on the porosity. Furthermore, $\bar{\boldsymbol{\sigma}} := \phi \boldsymbol{\sigma}_f + (1 - \phi)\boldsymbol{\sigma}_s$ with $\boldsymbol{\sigma}_f$ the fluid stress and $\boldsymbol{\sigma}_s$ the solid stress.

Equation (1) describes mass conservation for the solid phase, and equation (2) describes conservation of mass for the two-phase mixture. Equations (3) and (4) are linear momentum balances for the fluid phase and the two-phase mixture, respectively. It is assumed here that there is no mass transport between the two phases, i.e., no melting or recrystallization takes place, that the densities of the two phases are constant, and that gravitational forces are negligible.

We assume a Newtonian constitutive model for $\bar{\boldsymbol{\sigma}}$:

$$\bar{\boldsymbol{\sigma}} := -p_f\mathbf{I} + \zeta_\phi(\nabla\cdot\mathbf{u}_s)\mathbf{I} + \bar{\boldsymbol{\tau}}\,, \tag{5}$$

where ζ_ϕ is the effective bulk viscosity of the two-phase mixture and

$$\bar{\boldsymbol{\tau}} := \eta_\phi\left(\nabla\mathbf{u}_s + \nabla\mathbf{u}_s^T - \frac{2}{3}\left(\nabla\cdot\mathbf{u}_s\right)\mathbf{I}\right) \tag{6}$$

is the deviatoric stress; η_ϕ is the effective shear viscosity.

Inserting equation (3) into (2), under the preceding constitutive assumptions, equations (1)–(4) reduce to:

$$\frac{\partial\phi}{\partial t} + \nabla\cdot\left(1-\phi\right)\mathbf{u}_s = 0, \tag{7}$$

$$\nabla\cdot\left(-\frac{K_\phi}{\mu_f}\nabla p_f + \mathbf{u}_s\right) = 0, \tag{8}$$

$$-\nabla p_f + \nabla(\zeta_\phi\nabla\cdot\mathbf{u}_s) + \nabla\cdot\bar{\boldsymbol{\tau}} = \mathbf{0}, \tag{9}$$

where the primal unknowns are ϕ, p_f and $\mathbf{u}_s$.

To complete the problem, the following boundary conditions are applied:

$$-\frac{K_\phi}{\mu_f}\nabla p_f\cdot\mathbf{n} = 0 \text{ on } \partial\Omega\,, \tag{10}$$

$$\mathbf{u}_s = \mathbf{w} \text{ on } \partial\Omega\,, \tag{11}$$

where $\mathbf{w}$ is prescribed, and the boundaries are taken to be impermeable.

To non-dimensionalize the equations above, we use the following scalings:

$$\begin{gathered} K_\phi = K_0K'_\phi, \quad \mathbf{x} = H\mathbf{x}', \quad \mathbf{u_s} = H\dot{\gamma}\mathbf{u_s}', \quad t = \dot{\gamma}^{-1}t', \\ \eta_\phi = \eta_0\eta'_\phi, \quad \zeta_\phi = \zeta_0\zeta'_\phi, \quad p_f = \eta_0\dot{\gamma}p'_f, \end{gathered} \tag{12}$$

where ϕ_0 is the reference porosity, K_0 the permeability at the reference porosity, H a length measure and $\dot{\gamma}$ the imposed shear strain rate. The non-dimensional form of equations (7)–

(9) are:

$$\frac{\partial \phi}{\partial t'} + \nabla' \cdot (1-\phi)\, \mathbf{u}'_s = 0\,, \tag{13}$$

$$\nabla' \cdot \left(-\frac{D^2}{R+4/3} K'_\phi \nabla' p'_f + \mathbf{u}'_s \right) = 0\,, \tag{14}$$

$$\nabla' \cdot \left(2\eta'_\phi \bar{\boldsymbol{\epsilon}}(\mathbf{u}'_s) \right) + \nabla' \left(\left(R\zeta'_\phi - \frac{2}{3}\eta'_\phi \right) \nabla' \cdot \mathbf{u}'_s \right) - \nabla' p'_f = \mathbf{0}\,, \tag{15}$$

where $\bar{\boldsymbol{\epsilon}}(\mathbf{u}'_s) = (\nabla \mathbf{u}_s + \nabla \mathbf{u}_s^T)/2$ is the strain-rate tensor, the bulk-to-shear viscosity ratio $R = \zeta_0/\eta_0$ and the length scale $D = \delta/H$, in which

$$\delta = \sqrt{\frac{(R+4/3)\eta_0 K_0}{\mu_f}} \tag{16}$$

is the compaction length at reference porosity ϕ_0.

In this study, we choose the non-dimensional permeability K'_ϕ, bulk viscosity ζ'_ϕ and shear viscosity η'_ϕ to be:

$$K'_\phi = \left(\frac{\phi}{\phi_0}\right)^n, \quad \zeta'_\phi = \left(\frac{\phi}{\phi_0}\right)^{-m}, \quad \eta'_\phi = \mathrm{e}^{-\alpha(\phi-\phi_0)}, \tag{17}$$

with $n = 2$ and $m = 1$; the porosity-weakening exponent α and the bulk-to-shear viscosity ratio R are varied between simulations. The boundary conditions in non-dimensional form become:

$$-\frac{D^2}{R+4/3} K'_\phi \nabla' p'_f \cdot \mathbf{n}' = 0 \text{ on } \partial\Omega\,, \tag{18}$$

$$\mathbf{u}'_s = \mathbf{w}' \text{ on } \partial\Omega. \tag{19}$$

We dispense with the prime notation from this point and work at all times with the non-dimensional form.

3. Model Setup and Benchmarks

The governing equations in the previous section are solved using the finite element method. The finite element method is chosen for the ease with which arbitrarily shaped inclusions can be modeled and to permit localized spatial refinement. The developed finite element code builds on the open-source FEniCS Project libraries [*Logg et al.*, 2012; *Logg and Wells*, 2010], and the complete code for reproducing all examples in this work is freely available as supporting material. We summarize in this section some important aspects of the method that we use, and validate the model against published analytic and computational results.

3.1. Discretization

To solve the dimensionless governing equations (13)–(15), together with the boundary conditions in equation (18)–(19), using the finite element method we first cast the equations in a weak form. To handle the time derivative in the solution of the porosity evolution equation (13), the Crank-Nicolson scheme is used. For equations (14) and (15), the P^2–P^1 Taylor–Hood element on triangles is used. The weak forms and finite element scheme are detailed in Appendix A.

3.2. Boundary and Initial Conditions

Figure 1 shows a schematic of the domain and boundary conditions used for the simulations presented in Section 4. In all simulations, the top and bottom boundary are impermeable. The velocity is prescribed on these boundaries to create simple shear with the top moving to the right:

$$\mathbf{u}_s^{\text{top}}(x, H/2) = \left(\frac{H}{2}\dot{\gamma}, 0\right), \ \mathbf{u}_s^{\text{bottom}}(x, -H/2) = \left(-\frac{H}{2}\dot{\gamma}, 0\right), \tag{20}$$

where $\dot{\gamma}$ is the shear strain rate. The domain is periodic in the x-direction. In simulations with an inclusion, we additionally enforce zero net torque on the inclusion boundary using a Lagrange multiplier, and make the inclusion rotate as a rigid body using Nitsche's method (see Appendix B).

The simulations that are presented in Section 4 either have a uniform initial background porosity $\phi_0 = 0.05$, or a random initial field around $\phi_0 = 0.05$ with a maximum perturbation amplitude $A = 0.03$. This is within the range of initial porosities used in experiments [for example *Holtzman and Kohlstedt*, 2007; *Qi et al.*, 2013]. The random field is created once, and then re-used for all simulations to ensure reproducibility. The random initial perturbations in the porosity field are coarser than the grid scale, so that porosity variations are sufficiently resolved.

3.3. Rheology

The porosity-weakening exponent α (see equation (17)) has been experimentally determined to be around 26 for diffusion creep and 31 for dislocation creep [*Kelemen et al.*, 1997; *Mei et al.*, 2002]; $\alpha = 28$ has previously been used in simulations [e.g., *Katz et al.*, 2006]. In this study, we vary α between 0 and 50 so that we can establish, in detail, the effects of this porosity-weakening exponent on model dynamics.

The bulk-to-shear viscosity ratio R, however, is significantly less well-constrained. *Simpson et al.* [2010] used homogenization theory on two interpenetrating, viscously deformable fluids to deduce that the bulk-to-shear viscosity ratio R is proportional to the porosity as ϕ^{-1}, and consider $R \sim 20$ for a background porosity $\phi_0 = 0.05$. In contrast, *Takei and Holtzman* [2009] find, through a micro-scale model of diffusion creep of a grain partly wetted by melt, that $R \sim 5/3$, independent of porosity except when the porosity is vanishingly small (or when it is above the disaggregation fraction). In the simulations presented in Section 4, we use bulk-to-shear viscosities between 5/3 and 100 to encompass the values advocated in the above referenced studies.

With increasing strain, the amplitude of porosity variations is expected to grow. Given that there is no porosity-limiting term in the model, the porosity perturbations will grow to values beyond the mathematical bounds of zero and one. Therefore we terminate simulations when the porosity anywhere within the domain becomes smaller than zero or larger than one.

3.4. Benchmark 1: Instantaneous Compaction Around a Circle

The instantaneous compaction around a circular inclusion in a medium with a uniform initial porosity has been described analytically by *Rudge* [2013] and therefore lends itself as a benchmark for numerical simulations of compaction.

The far field velocity consists of simple shear and can be written as $\mathbf{u}_\infty = (\dot{\gamma} y, 0)$ in terms of a strain rate $\dot{\gamma}$. The governing equations (13)–(15) are solved with $\mathbf{u}_s = \mathbf{0}$ and $\nabla p_f \cdot \mathbf{n} = 0$ on the circle. This results in the following analytical solutions for matrix velocity $\mathbf{u}_s$ and pressure p_f [*Rudge*, 2013]:

$$\mathbf{u}_s = \mathbf{u}_\infty + \left(-\frac{4G}{r^4} + \frac{2HK_2(r)}{r^2} \right) \mathbf{E} \cdot \mathbf{x} + \left(-\frac{2F}{r^4} + \frac{8G}{r^6} - \frac{HK_3(r)}{r^3} \right) (\mathbf{x} \cdot \mathbf{E} \cdot \mathbf{x}) \mathbf{x} \,, \quad (21)$$

$$p_f = \left(-\frac{4\mathcal{B}F}{r^4} + \frac{HK_2(r)}{r^2} \right) \mathbf{x} \cdot \mathbf{E} \cdot \mathbf{x} \,, \quad (22)$$

where $K_n(r)$ is the modified Bessel function of the second kind, $\mathcal{B} = \eta/(\zeta + (4/3)\eta)$, and

$$F = -\frac{a^4 K_2'(a)}{4\mathcal{B}K_1(a) - a^2 K_2'(a)}, \tag{23}$$

$$G = \frac{a^4}{4} + \frac{4a^3\mathcal{B}K_2(a)}{4\mathcal{B}K_1(a) - a^2 K_2'(a)}, \tag{24}$$

$$H = \frac{8a\mathcal{B}}{4\mathcal{B}K_1(a) - a^2 K_2'(a)}, \tag{25}$$

where r is the distance from the center of the inclusion and a the radius of the circle. This solution assumes a finite compaction length δ, and all lengths have been scaled with the compaction length.

$\mathbf{E}$ is the constant, trace-free, symmetric, second-rank, strain rate tensor of the far-field flow, $\mathbf{E} = \frac{1}{2}\left(\nabla \mathbf{u}_\infty + \nabla \mathbf{u}_\infty^T\right)$, which can be written in components as

$$\mathbf{E} = \frac{1}{2}\begin{pmatrix} 0 & \dot{\gamma} \\ \dot{\gamma} & 0 \end{pmatrix}. \tag{26}$$

The compaction rate is:

$$\nabla \cdot \mathbf{u}_s = \frac{F K_2(r)}{r^2}\mathbf{x} \cdot \mathbf{E} \cdot \mathbf{x}\,. \tag{27}$$

Figure 2a shows the antisymmetric pattern of the instantaneous compaction rate, with two positive and two negative lobes around the circle in the shape of a quadrupole. The negative compaction rate lobes form where overpressure causes melt to be expelled, leading to compaction and therefore low porosity. The positive lobes have an underpressure, and therefore attract melt and decompact, resulting in high porosity.

To validate the numerical results, we compute the L_2 difference e between the numerical solid velocity field $\mathbf{u}_s^N$ and the analytical solution $\mathbf{u}_s^A$ given in equation (21):

$$e = \frac{||\mathbf{u}_s^N - \mathbf{u}_s^A||_2}{||\mathbf{u}_s^A||}, \tag{28}$$

for different radii of the inclusion a. The results are shown in Figure 2b. The analytical solution assumes an infinite domain, whereas the numerical solution is affected by the boundaries at the top and bottom. These boundary effects (and therefore e) are reduced if the size of the inclusion is decreased relative to the domain size while still resolving the compaction around the inclusion.

3.5. Benchmark 2: Plane Wave Melt Bands

We will now look at the angle and growth of melt bands as they rotate under simple shear in a rectangular, two-dimensional domain with aspect ratio 4. This benchmark aims to reproduce analytical solutions of initial melt band growth rate [*Spiegelman*, 2003].

The initial condition for this benchmark is a plane wave in the porosity field, described by:

$$\phi_{\text{init}}(x, y) = 1.0 + A\cos\big(k_0 x \sin(\theta_0) + k_0 y \cos(\theta_0)\big) \tag{29}$$

The wavenumber and melt band angle at $t = 0$ are given by $k_0 = |\mathbf{k}|_{t=0}$ and $\theta_0 = \tan^{-1}[k_x^0/k_y^0]$, respectively. The amplitude of the perturbation (A) must be small for the linear approximation in the analytical solution to be valid. The analytical solution for melt band growth rates is [*Spiegelman*, 2003]:

$$\dot{s}_A = -\frac{\eta_0}{\zeta_0 + (4/3)\eta_0}\alpha(1-\phi_0)2\dot{\varepsilon}_{xy}\sin 2\theta\,. \tag{30}$$

The strain rate $\dot{\varepsilon}_{xy}$ is equal to 1/2 for simple shear. The numerical melt band growth rate is computed as follows:

$$\dot{s}_N = \frac{(1-\phi_0)}{A\phi_0}\nabla\cdot\mathbf{u_s}\,. \tag{31}$$

Figure 3 shows the melt bands rotating with increasing shear, i.e., with progressing time. The band angle $\theta(t)$ is given by [*Katz et al.*, 2006]:

$$\theta(t) = \tan^{-1}\left[\frac{\sin\theta_0}{\cos\theta_0 - t\sin\theta_0}\right]. \tag{32}$$

We first validate the numerical results by comparing numerical and analytical growth rates for different initial melt-band angles θ_0. Figure 4a displays a sinusoidal dependence on θ_0. Figure 4b shows that the numerical error in the growth rate decreases with decreasing grid spacing h and with decreasing wavenumber k_0. A higher wavenumber results in narrower melt bands, and therefore requires smaller grid cells in order to be sufficiently resolved. The rate of convergence is approximately of order $\mathcal{O}(h^2)$ in both cases.

The analytical solution is valid only when perturbations in the porosity field are small, which becomes apparent when the perturbation amplitude is increased, as shown in Figure 4c. The difference between the numerical and analytical growth rates becomes significant for amplitudes $\geq 10^{-2}$. Hence the analytical solution does not hold under experimental conditions where perturbations have magnitudes of $\mathcal{O}(10^{-2})$ to $\mathcal{O}(10^{-1})$. This is unsurprising given the that analytical growth rate is obtained by linearizing the governing equations about a uniform-porosity state.

4. Results

We now present three model problems of increasing complexity. First, we consider melt bands in a partially molten medium without an inclusion but with a randomly perturbed initial porosity field. Then we investigate the compaction pattern around a circular inclusion in an initially uniform porosity field. Finally, we combine a randomly perturbed initial porosity field with a circular inclusion.

The simulations presented in Section 4 with no inclusion are solved on a uniform square mesh with 300×300 cells, such that the cell size is approximately 5×10^{-3}. Simulations with an inclusion have a mesh that is linearly refined towards the inclusion boundary, with cell sizes ranging from 1×10^{-2} near the outer boundaries to 2×10^{-3} near the inclusion.

4.1. Melt Bands in a Random Medium Without an Inclusion

For a partially molten medium without any inclusions, we consider a random initial porosity field with a perturbation amplitude of 0.03 with a background value of 0.05 (Figure 5a). We study a suite of simulations with a wide range of values for the porosity-weakening exponent ($\alpha \in [15, 50]$) and bulk-to-shear viscosity ratio ($R \in [1.7, 100]$) in order to establish the parameter regime for which melt-rich bands readily develop. For this case, we do not consider simulations with $\alpha = 0$, since a positive porosity-weakening exponent is required for a non-zero melt band growth rate (see equation (30)).

Figure 5c-d shows that for $\alpha = 28$ and a small bulk-to-shear viscosity ratio R of 1.7, high-porosity bands form rapidly, and are well-developed at a strain of 0.1. The bands rotate clockwise in the simple shear velocity field, but continue to re-form at 45°. The bands with positive compaction rate and high porosity dominate over the negative compaction rate and low-porosity features due to the porosity weakening rheology.

For $R = 20$, melt bands have not fully formed yet at a strain of 0.5, as shown in Figure 5e-f. Even though bands are not widely present in the porosity field, the high compaction rate areas are concentrated in narrow bands at 45° to the plane of shear. As melt bands grow more slowly for higher bulk-to-shear viscosity ratios (see equation (30)), the re-forming at a 45° angle happens at a slower rate, and small parts of the bands in the compaction rate field have therefore a higher angle than for the $R = 1.7$ case.

A small bulk-to-shear viscosity ratio ($R \leq 10$) and a large porosity-weakening exponent are required to form persistent shear bands. Both factors enhance melt band growth rates, and thus cause the porosity to exceed the physical range of $[0, 1]$ more rapidly. We therefore conclude from these simulations that it is challenging to obtain simulations with well-developed melt bands at high strains while keeping the porosity within physical bounds.

4.2. Compaction Around an Inclusion with Uniform Initial Porosity

We now introduce a circular inclusion into the domain. With a uniform initial porosity, the instantaneous compaction rate at a strain of zero is identical to the pattern shown in Figure 2a (Benchmark 1). When a medium with $\alpha = 0$ and $R = 50$ is deformed by simple shear, the porosity field initially develops according to this instantaneous compaction rate pattern as indicated in Figure 6a-b. As the strain increases, the porosity lobes rotate around the inclusion according to the simple shear velocity field. Figures 6c and 6e show that the high-porosity lobes become stretched, and grow faster and into sharper features than the low-porosity lobes. Even though the porosity exponent in the shear viscosity is zero in the case shown here, the permeability and bulk viscosity still depend on porosity (see equation (17)).

The compaction rate evolves in a different manner than the porosity. The divergence of the velocity field is mainly governed by the prescribed constant simple shear. Hence the non-rotating instantaneous pattern generally dominates, as illustrated in Figure 6b. At high strains, the compaction rate is affected by the large porosity variations that have developed. Figures 6d and f show that the areas with highest porosity and therefore lowest bulk viscosity are most easily deformed, partially overprinting the instantaneous pattern, which results in deformed compaction rate lobes.

To further analyze the evolution of porosity and compaction rate, we compute integrals of ϕ and $\nabla \cdot \mathbf{u}_s$ from the boundary of the inclusion at radius $r = a$ outward to a radius of $r = 2a$, for a series of azimuths between 0 and 2π:

$$\frac{1}{a}\int_a^{2a} \phi \, \mathrm{dr}, \qquad \frac{1}{a}\int_a^{2a} (\nabla \cdot \mathbf{u}_s) \, \mathrm{dr}. \tag{33}$$

These integrals show the rotation and evolution of the asymmetry of the high- and low-porosity lobes in Figure 6g, and the deformation of features in the compaction rate field in Figure 6h.

Both the bulk-to-shear viscosity ratio R and the porosity-weakening exponent α in the shear viscosity have a profound effect on the porosity evolution and compaction rate. A smaller bulk-to-shear viscosity ratio results in faster and more asymmetric growth of features in the porosity field, and causes the porosity to go out of bounds more quickly. For example, the simulation with $R = 1.7$ and $\alpha = 0$ in Figure 7a and c shows a similar porosity field as the case with $R = 50$ but with larger amplitudes. The compaction rate field is more strongly affected by the porosity for smaller R because the porosity differences in space are larger. A low porosity acts to decrease the compaction rate. As the porosity lobes rotate with shear and become misaligned with the non-rotating compaction rate lobes, they decrease the magnitude of negative compaction rate lobes in an asymmetric manner (Figure 7b, d). This simulation goes out of physical bounds for a strain > 0.3.

In the small bulk-to-shear viscosity regime, the effect of the porosity exponent α is particularly discernible. When α is chosen to be the experimentally determined value of 28, the porosity reaches the physical limits at an even smaller strain of 0.1. The porosity and compaction rate features in Figure 8 develop similar to the melt bands seen in the previous section, with an elongated shape towards 45° from the plane of shear. The maximum value of the compaction rate grows with time when $\alpha > 0$, and its peaks flatten with the widening high-compaction rate lobes.

Figure 9 summarizes the controlling effect of R and α; for $\alpha = 0$, increasing R causes compaction around the inclusion to have larger amplitudes, resulting in sharper positive porosity lobes (that are advected, Figure 9a) and deformed negative compaction rate lobes (Figure 9b). Figure 9c-d shows that when $\alpha = 28$, a higher R results in wider and flatter positive lobes in porosity and compaction rate, indicating behavior similar to melt bands.

4.3. Melt Bands and Pressure Shadows Around an Inclusion

The final suite of tests involves a random initial porosity field around the inclusion. Generally, the porosity goes out of bounds significantly faster than in the preceding tests, as the compaction around the inclusion compounds the growth of porosity in melt bands. Figure 10a shows that this results in less extensive melt bands, even with high α and low R where, at most, short high-porosity bands can be seen adjacent to the inclusion for a case with $\alpha = 28$ and $R = 1.7$. The compaction rate shows both the bands and the effect of the inclusion (Figure 10b). In the integrals, melt bands distinguish themselves by peaks that flatten with strain, whereas pressure shadows around the inclusion manifest themselves as a sinusoidal quadrupole shape. Figure 10c indicates that the porosity amplitudes increase as the positive lobes grow faster with increasing strain. In the compaction rate field in Figure 10d, only the positive lobes grow. An increase in R causes melt bands to grow more slowly, and compaction around the inclusion to be dominant over domain-wide melt bands, as shown in Figure 11a-b. This is especially reflected in the porosity and compaction rate integrals in Figures 11c-d and 12 which, for large R, closely resemble the uniform case with wide troughs and sharp peaks.

4.4. Model regimes

The results of the three sets of simulations are summarized as a function of the porosity exponent α and bulk-to-shear viscosity ratio R in Figure 13. The maximum strain $\gamma_{\max}$ reached in simulations is an indicator for the effective growth rate brought about by all melt segregation processes together. Generally, $\gamma_{\max}$ increases with decreasing effective growth rate, i.e., with increasing R and decreasing α, indicated by the black contours in Figure 13. Figure 13a shows that simulations with uniform initial porosity and with only linear compaction around an inclusion evolve to the largest strains of the three suites. The maximum strain is the lowest in simulations where compaction around the inclusion competes with the exponential growth of melt bands originating in the random initial porosity field, as indicated in Figure 13c.

For the simulations with uniform initial porosity, we compute the average width W of the two high-porosity lobes around the inclusion at the final strain scaled by 0.5π (the width of a lobe in its initial state), shown as the color background in Figure 13a. A scaled lobe width larger than one indicates flattened high-porosity lobes and narrow low-porosity lobes, and therefore shearing, such as in Figure 8a. On the other hand, $W < 1$ indicates that the high-porosity lobes are narrow and advected according to the simple shear velocity field, as for example in Figure 6e. The lobe width increases with α and decreases with R, and is inversely proportional to the maximum strain, demonstrated by the contours of W that parallel those of maximum strain. Therefore W must be proportional to the growth rate of porosity anomalies.

A scaled lobe width $W > 1$ is seen for $R \leq 10$ when $\alpha > 15$, and for $R \leq 5$ when $\alpha = 15$. This could be viewed as the regime where melt-rich bands could develop. For small R and large α, W decreases again; this indicates the underdevelopment of porosity lobes for small maximum strain.

In simulations with random initial porosity without a inclusion, melt bands are seen for $R < 20$ when $\alpha < 50$, and for $R \leq 20$ when $\alpha = 50$ (indicated by the green circles in Figure 13b). Figure 13c shows that in simulations with random initial porosity and a circular inclusion, melt bands are more elusive and only develop for $R < 5$ and $\alpha > 15$. Outside this narrow regime, the porosity field is dominated by compaction around the inclusion.

5. Discussion

The numerical models of partially molten mantle material presented in this paper explore the evolution of melt segregation as a function of the bulk-to-shear viscosity ratio R and the porosity-weakening exponent of the shear viscosity α. These parameters control the balance between pressure shadows around an inclusion and domain-wide melt bands. Generally, the pressure shadows around the inclusion dominate the porosity field. There is a small portion of the parameter regime that allows for significant development of melt bands, requiring a small bulk-to-shear viscosity ratio and therefore a material that is relatively easily compactable.

The porosity field that represents the melt distribution in the simulations does not bear close resemblance to the experimental results obtained by *Qi et al.* [2013]. Most importantly, we are not able to reproduce prominent melt bands adjacent to the inclusion, that overprint the pressure shadows around the inclusion. Secondly, the strains at which the porosity in the simulations exceeds the physical regime of $[0, 1]$ are significantly smaller than those at which the experiments fail. *Qi et al.* [2013] report maximum local strains between 0.9 and 5.0, whereas in our numerical simulations with a random initial porosity around an inclusion the maximum strains are between 0.03 and 0.8. Furthermore, when the porosity increases past ~ 0.25 in partially molten rock, it disaggregates and the solid particles are in suspension. We do not consider these processes in our numerical models since laboratory experiments are terminated before reaching the disaggregate regime.

In our simulations, the presence of an inclusion causes the porosity to go out of bounds more quickly, as the compaction in pressure shadows around the inclusion compounds the porosity growth in melt bands directly adjacent to the inclusion. For the same total strain, simulations with and without a circular inclusion show the same amount of melt band development, indicating that the lack of melt bands in simulations with the inclusion compared to the simulations without the inclusion is exclusively the result of a smaller maximum strain. The exact maximum strain reached in a simulation is not necessarily relevant, as it may depend on the placement of the initial random high-porosity perturbations directly adjacent to the inclusion. Rather the observed trends in maximum strains as a function of model parameters inform us about the effective growth rates of porosity near the inclusion as a result of the two competing modes of melt segregation.

The porosity going out of bounds is indicative of physics not captured by the set of governing equations and constitutive relations presented in this paper. Several studies suggest possible modifications to constitutive relations that would limit the growth of sharp porosity gradients. For example, *Bercovici et al.* [2001] use surface tension terms, and *Takei and Hier-Majumder* [2009] consider a second melt segregation process aside from decompaction and compaction of the solid that results from dissolution and precipitation in the melt. *Keller et al.* [2013] implement a higher-order polynomial form for the porosity-dependent permeability that results in a decrease in permeability for very high porosities. The most appropriate approach to this question remains a debate; more theoretical work is likely needed to resolve it. Incorporation of mechanisms that prevent the porosity going out of bounds at small strains could lead to a larger parameter space for which simulations display melt bands than indicated in this paper.

Melt-rich bands are observed to form at shallow angles of 15-20° [*Holtzman et al.*, 2003; *Holtzman and Kohlstedt*, 2007; *King et al.*, 2010; *Qi et al.*, 2013]. In numerical models, melt bands form at 45° angle to the simple shear plane, unless a non-Newtonian rheology with large stress exponent ($n > 3$) [*Katz et al.*, 2006] or an anisotropic viscosity is used [*Takei and Katz*, 2013; *Katz and Takei*, 2013]. In this work, we are primarily concerned with understanding the model behavior as function of the bulk-to-shear viscosity ratio and the porosity-weakening exponent. The incorporation of non-Newtonian and anisotropic viscosities is a topic of ongoing work, and should improve comparisons of our simulations with experimental results.

An important feature of laboratory experiments is their three-dimensional nature. Numerical simulations should also be performed in three dimensions to advance a detailed quantitative comparison with experimental results. The compaction rate around a circular inclusion in two dimensions decays as $1/r^2$ and around a spherical inclusion in three dimensions as $1/r^3$. We therefore expect pressure shadows to be spatially limited in three-dimensional models, which could allow planar melt bands to become more prominent. However, such computations in three dimensions are computationally challenging as they involve very large systems of equations. The key to tractable simulations in three dimensions is the development of effective preconditioners to accelerate the solution of linear systems. Research in this area is underway [*Rhebergen et al.*, 2013], and the implementation and use of recently developed preconditioners will enable three-dimensional computations of two-phase flow at high resolutions, which will be the core of future work.

6. Conclusions

We computed two-dimensional models of partially molten mantle material under simple shear, with and without inclusions that perturb the flow. The model configurations are based on recent laboratory experiments that exhibit pressure shadows around an inclusion and associated melt bands as competing features in the melt distribution. Previous theoretical studies only considered instantaneous solutions to the governing equations; we improve on this by computing the evolution of the two-phase material with strain. The simulations display the pressure shadows around a circular inclusion, as well as abundant melt band development in simulations without an inclusion. The geometry and evolution of these features depend on the bulk-to-shear viscosity ratio as well as on the porosity-weakening exponent in the shear viscosity. However, it has proven challenging to determine a parameter regime for which melt bands develop in the presence of an inclusion. We find that a bulk-to-shear viscosity ratio of less than 5 is required in our simulations. For such small bulk-to-shear viscosity ratios, the porosity field reaches its physical bounds at unrealistically small strains. This indicates that an important component of the physics is not captured in the governing equations and constitutive relations outlined in this paper, and some form of limiter on porosity weakening would be required to obtain numerical results that resemble the laboratory experiments more closely.

Appendix A: Weak Form

To solve equations (13)–(15), together with boundary conditions in equation (18)–(19), we cast them in a weak form. Given ϕ, the weak solutions $\mathbf{u}_s$ and p_f satisfy

$$\begin{aligned}0 = \int_\Omega 2\eta_\phi \overline{\boldsymbol{\epsilon}}(\mathbf{u}_s) : \overline{\boldsymbol{\epsilon}}(\mathbf{v}_s)\,\mathrm{dx} \; + \int_\Omega (R\zeta_\phi - \tfrac{2}{3}\eta_\phi)(\nabla \cdot \mathbf{u}_s)(\nabla \cdot \mathbf{v}_s)\,\mathrm{dx} \\ - \int_\Omega p_f \nabla \cdot \mathbf{v}_s\,\mathrm{dx} - \int_\Omega q_f \nabla \cdot \mathbf{u}_s\,\mathrm{dx} - \int_\Omega \left(\frac{D^2}{R+4/3}\right) K_\phi \nabla p_f \cdot \nabla q_f\,\mathrm{dx},\end{aligned} \quad \text{(A1)}$$

where $\mathbf{v}_s$ and q_f are arbitrary test functions. To obtain the weak form of equation (13) it will be useful to first discretize in time. We use a Crank-Nicolson time stepping scheme:

$$\phi - \phi^0 + \Delta t \left(\mathbf{u_s} \cdot \nabla \phi^{\mathrm{mid}} - (1-\phi^{\mathrm{mid}})\nabla \cdot \mathbf{u}_s\right) = 0, \quad \text{(A2)}$$

where Δt is the time step, $\phi^{\mathrm{mid}} = \frac{1}{2}(\phi + \phi^0)$ and ϕ^0 and ϕ are, respectively, the known and unknown porosities from the previous and current time step. Given $\mathbf{u}_s$ from the previous time step, the weak solution ϕ satisfies

$$0 = \int_\Omega w \left(\phi - \phi^0 + \Delta t \left(\mathbf{u_s} \cdot \nabla \phi^{\mathrm{mid}} - (1-\phi^{\mathrm{mid}})\nabla \cdot \mathbf{u}_s\right)\right)\,\mathrm{dx}, \quad \text{(A3)}$$

where w is an arbitrary test function.

Additionally, we apply standard streamline upwind Petrov-Galerkin stabilization by adding a term r_{SUPG} to the porosity transport equation (A3) [*Brooks and Hughes*, 1982]:

$$k_{\mathrm{eff}} = \frac{1}{2}\left(\frac{h|\mathbf{u}_s|}{2} - 1 + \left|\frac{h|\mathbf{u}_s|}{2} - 1\right|\right) \quad \text{(A4)}$$

$$r_{\mathrm{SUPG}} = \int_\Omega \frac{k_{\mathrm{eff}}}{|\mathbf{u}_s|^2}\,(\mathbf{u}_s \cdot \nabla w)\, r_{\mathrm{CN}}\,\mathrm{dx}, \quad \text{(A5)}$$

where h is the cell size, $|\mathbf{u}_s|$ is the norm of the solid velocity field, and r_{CN} is the residual of equation (A3).

Appendix B: Boundary Conditions on the Inclusion

We impose a no-net torque boundary condition on the circular inclusion:

$$\int_{\Omega_s} \mathbf{x} \times (\bar{\boldsymbol{\sigma}} \cdot \mathbf{n}) \, \mathrm{ds} = \mathbf{0} \tag{B1}$$

which is applied by adding a term F_{L} to the weak form in equation (A1):

$$F_{\mathrm{L}} = \boldsymbol{\lambda} \cdot \int_{\Omega_s} \mathbf{x} \times (\bar{\boldsymbol{\sigma}} \cdot \mathbf{n}) \, \mathrm{ds}, \tag{B2}$$

where $\boldsymbol{\lambda}$ is the Lagrange multiplier, which reduces to $(0, 0, \lambda)$ in our two-dimensional model.

The second boundary condition on the inclusion is a rigid body rotation. Nitsche's method is used to ensure that $\mathbf{u}_s = \boldsymbol{\omega} \times \mathbf{x}$ on the inclusion boundary. This is a variationally consistent method for the weak imposition of Dirichlet boundary conditions, consisting of a term F_{N} added to the weak form in equation (A1):

$$F_{\mathrm{N}} = \int_{\Omega_s} \frac{10}{h} (\mathbf{u}_s - \boldsymbol{\omega} \times \mathbf{x}) \cdot \mathbf{v}_s - (\mathbf{u}_s - \boldsymbol{\omega} \times \mathbf{x}) \cdot \mathbf{t}_v - \mathbf{v}_s \cdot \mathbf{t}_u \, \mathrm{ds} \tag{B3}$$

where h is the cell size, and $\boldsymbol{\omega}$ is the unknown rotation rate of the inclusion. $\mathbf{t}_u$ and $\mathbf{t}_v$ are traction vectors $(\bar{\boldsymbol{\sigma}} \cdot \mathbf{n})$ corresponding to velocities $\mathbf{u}_s$ and $\mathbf{v}_s$. For the simulations presented here, $\boldsymbol{\omega} = (0, 0, \omega)$.

Acknowledgments. This work was supported by the Natural Environment Research Council under grants NE/I023929/1 and NE/I026995/1. We would like to thank Chao Qi and David Kohlstedt for discussions of their experimental results. Katz thanks the Leverhulme Trust for support.

References

Bercovici, D., Y. Ricard, and G. Schubert (2001), A two-phase model for compaction and damage 1. General theory, *Journal Of Geophysical Research*, *106*, 8887–8906.

Brooks, A. N., and T. J. R. Hughes (1982), Streamline upwind/Petrov–Galerkin formulations for convection dominated flows with particular emphasis on the incompressible Navier–Stokes equations, *Comput. Methods Appl. Mech. Eng.*, *32*, 199–259.

Butler, S. L. (2009), The effects of buoyancy on shear-induced melt bands in a compacting porous medium, *Phys. Earth Planet. In.*, *173*(1-2), 51–59, doi:10.1016/j.pepi.2008.10.022.

Butler, S. L. (2010), Porosity localizing instability in a compacting porous layer in a pure shear flow and the evolution of porosity band wavelength, *Phys. Earth Planet. In.*, *182*, 30–41, doi:10.1016/j.pepi.2010.06.004.

Holtzman, B. K., and D. L. Kohlstedt (2007), Stress-driven melt segregation and strain partitioning in partially molten rocks: Effects of stress and strain, *J. Petrology*, *48*(12), 2379–2406, doi:10.1093/petrology/egm065.

Holtzman, B. K., N. J. Groebner, M. E. Zimmerman, S. Ginsberg, and D. Kohlstedt (2003), Stress-driven melt segregation in partially molten rocks, *Geochem. Geophys. Geosys.*, *4*, doi:10.1029/2001GC000258.

Katz, R. F., and Y. Takei (2013), Consequences of viscous anisotropy in a deforming, two-phase aggregate: 2. Numerical solutions of the full equations, *Journal of Fluid Mechanics*, *734*, 456–485, doi:10.1017/jfm.2013.483.

Katz, R. F., M. Spiegelman, and B. Holtzman (2006), The dynamics of melt and shear localization in partially molten aggregates, *Nature*, *442*, 676–679, doi:10.1038/

nature05039.

Kelemen, P. B., G. Hirth, N. Shimizu, M. Spiegelman, and H. J. B. Dick (1997), A review of melt migration processes in the adiabatically upwelling mantle beneath oceanic spreading ridges, *Phil. Trans. R. Soc. London A*, *355*(1723), 283–318.

Keller, T., D. A. May, and B. J. P. Kaus (2013), Numerical modelling of magma dynamics coupled to tectonic deformation of lithosphere and crust, *Geophysical Journal International*, *195*(3), doi:10.1093/gji/ggt306.

King, D. S. H., M. E. Zimmerman, and D. L. Kohlstedt (2010), Stress-driven melt segregation in partially molten olivine-rich rocks deformed in torsion, *J. Petrol.*, *51*, 21–42, doi:10.1093/petrology/egp062.

Logg, A., and G. N. Wells (2010), DOLFIN: Automated finite element computing, *ACM Trans. Math. Software*, *37*(2), 20:1–20:28, doi:10.1145/1731022.1731030.

Logg, A., K.-A. Mardal, and G. N. Wells (Eds.) (2012), *Automated Solution of Differential Equations by the Finite Element Method*, *Lecture Notes in Computational Science and Engineering*, vol. 84, Springer, doi:10.1007/978-3-642-23099-8.

McKenzie, D. (1984), The generation and compaction of partially molten rock, *Journal of Petrology*, *25*, 713–765, doi:10.1093/petrology/25.3.713.

McKenzie, D., and M. Holness (2000), Local deformation in compacting flows: Development of pressure shadows, *Earth And Planetary Science Letters*, *180*, 169–184.

Mei, S., W. Bai, T. Hiraga, and D. Kohlstedt (2002), Influence of melt on the creep behavior of olivinebasalt aggregates under hydrous conditions, *Earth and Planetary Science Letters*, *201*(3), 491–507.

Qi, C., Y.-H. Zhao, and D. L. Kohlstedt (2013), An experimental study of pressure shadows in partially molten rocks, *Earth and Planetary Science Letters*, *382*, 77–84, doi: 10.1016/j.epsl.2013.09.004.

Rhebergen, S., G. N. Wells, R. F. Katz, and A. J. Wathen (2013), An optimal preconditioner for models of coupled magma/mantle dynamics, http://arxiv.org/abs/1311.6372.

Rudge, J. F. (2013), Analytical solutions of compacting flow past a sphere, *Journal of Fluid Mechanics*, in revision. Preprint available at http://www.johnrudge.com.

Simpson, G., M. Spiegelman, and M. I. Weinstein (2010), A multiscale model of partial melts: 2. Numerical results, *Journal Of Geophysical Research*, *115*, doi:10.1029/2009JB006376.

Spiegelman, M. (2003), Linear analysis of melt band formation by simple shear, *Geochemistry, Geophysics, Geosystems*, *4*(9), 8615, doi:10.1029/2002GC000499.

Stevenson, D. J. (1989), Spontaneous small-scale melt segregation in partial melts undergoing deformation, *Geophysical Research Letters*, *16*, 1067–1070.

Takei, Y., and S. Hier-Majumder (2009), A generalized formulation of interfacial tension driven fluid migration with dissolution/precipitation, *Earth and Planetary Science Letters*, *288*, 138–148, doi:10.1016/j.epsl.2009.09.016.

Takei, Y., and B. K. Holtzman (2009), Viscous constitutive relations of solid-liquid composites in terms of grain boundary contiguity: 1. Grain boundary diffusion control model, *Journal Of Geophysical Research*, *114*, doi:10.1029/2008JB005850.

Takei, Y., and R. F. Katz (2013), Consequences of viscous anisotropy in a deforming, two-phase aggregate: 1. Governing equations and linearised analysis, *Journal of Fluid*

Mechanics, *734*, 456–485, doi:10.1017/jfm.2013.483.

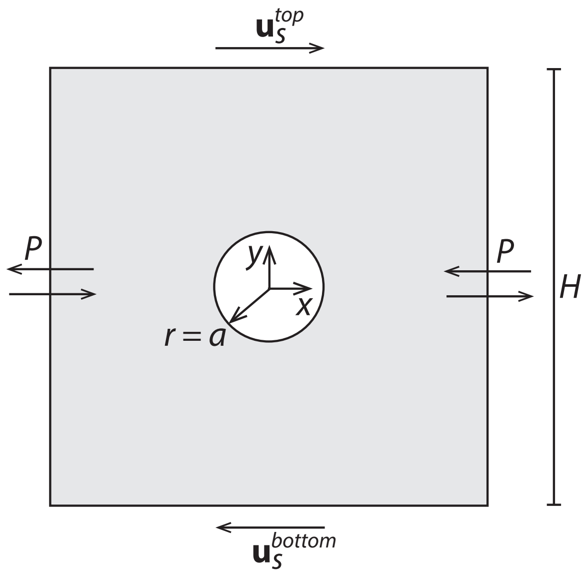

Figure 1. Schematic of the domain and boundary conditions used for the simulations presented in Section 4. The side boundaries indicated by P are periodic; the top and bottom boundaries have a prescribed horizontal velocity. The height of the domain is indicated by H, and the radius of the inclusion around the origin is given by a.

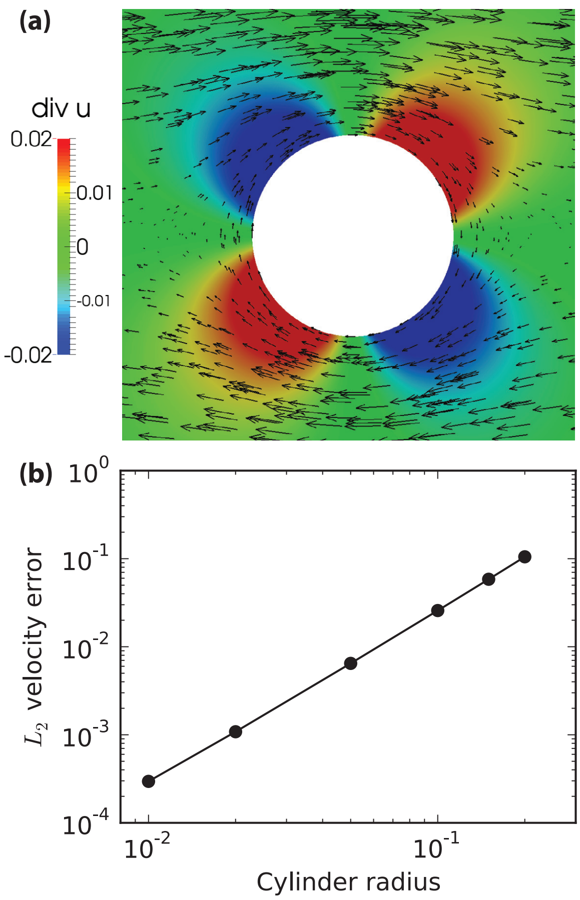

Figure 2. (a) Instantaneous compaction pattern around a circular inclusion under simple shear (only a part of the full domain is shown). The top moves to the right, the bottom to the left. (b) L_2 difference e between the analytical and numerical velocity field, for various inclusion radii, with a mesh of 160×160 cells. The inclusion radius a is given as a fraction of the height of the domain.

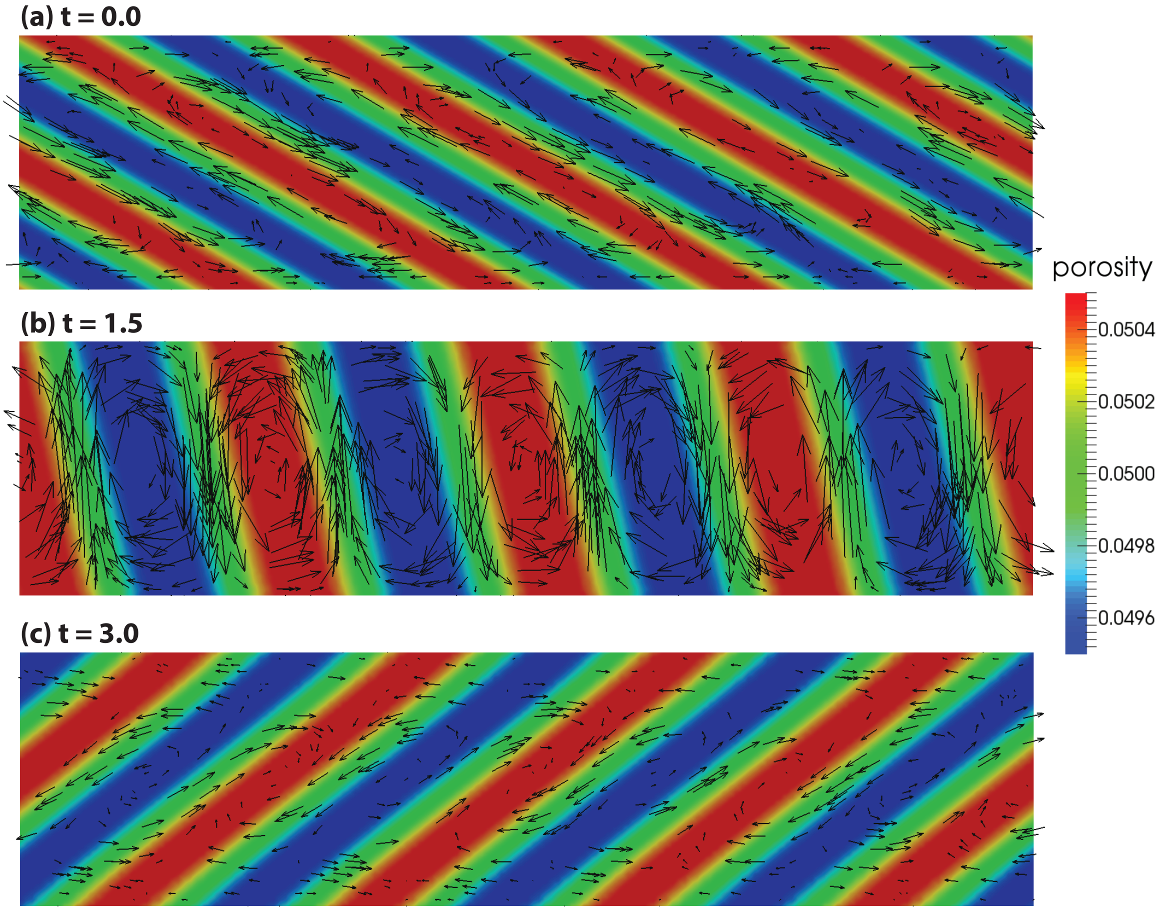

Figure 3. Plane wave porosity field at strains of (a) 0.0, (b) 1.5, and (c) 3.0. The top boundary moves to the right, the bottom boundary to the left. The arrows show the perturbations in the solid velocity with respect to the simple shear velocity field.

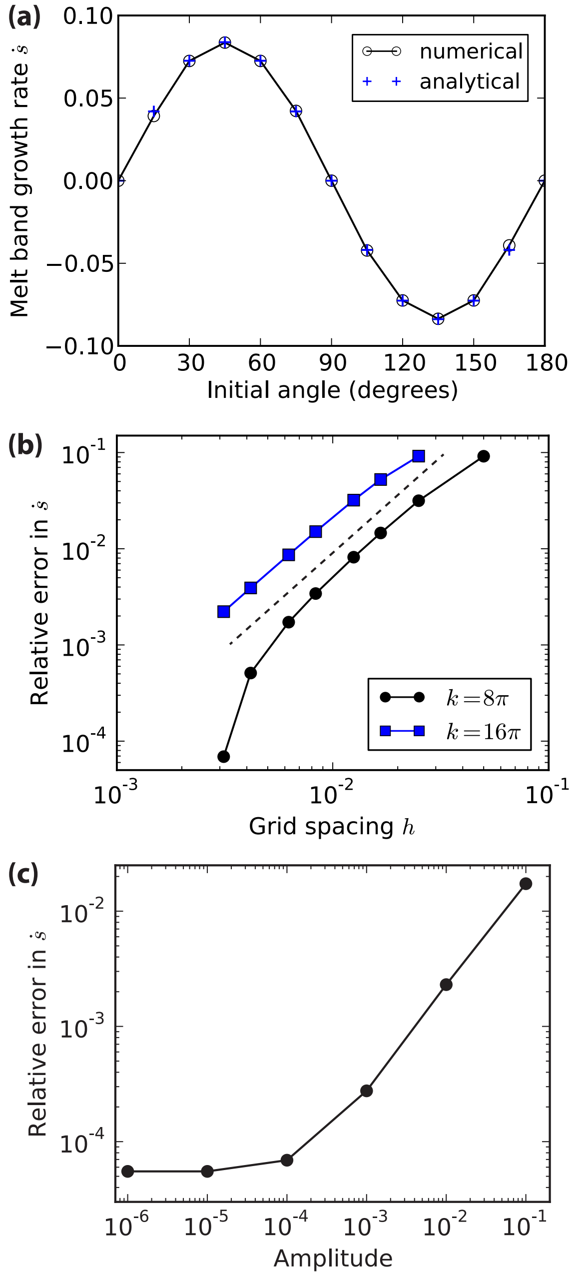

Figure 4. (a) Initial melt band growth rate for various initial melt band angles, with porosity amplitude $A = 10^{-4}$, wavenumber $k_0 = 4\pi$, and number of grid points along the short side $n = 80$. (b) Relative error in initial melt band growth rate as a function of grid spacing $h = 1/n$ for $k_0 = 8\pi$ and 16π; $\theta_0 = 30°$. The dotted line indicates an order $\mathcal{O}(h^2)$ convergence. (c) Relative error in initial melt band growth rate for various porosity perturbation amplitudes, with $n = 80$ and $k_0 = 4\pi$. For all simulations shown: porosity-weakening exponent $\alpha = 1$, background porosity $\phi_0 = 0.05$, bulk-to-shear viscosity ratio $R = 10$, and the compaction length $\delta = 1$.

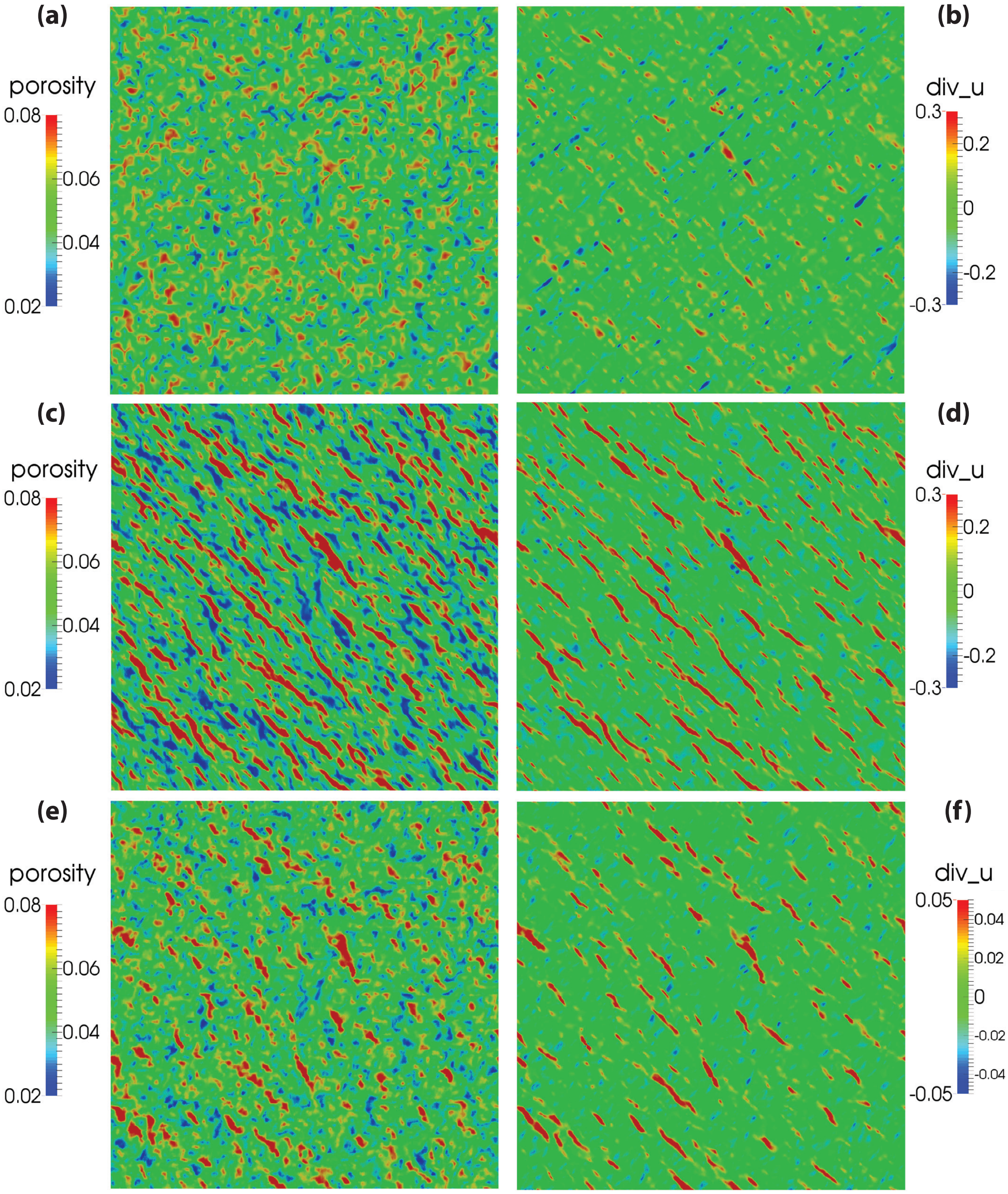

Figure 5. (a) Porosity and (b) compaction rate in a partially molten medium with random initial porosity under simple shear without inclusion, $\alpha = 28$ and $R = 1.7$, at its initial state. (c) Porosity and (d) compaction rate for the same simulation, at a strain of 0.1. (e) Porosity and (f) compaction rate for a simulation with $R = 20$ at a strain of 0.5. In all cases, the top boundary moves to the right and the bottom boundary to the left.

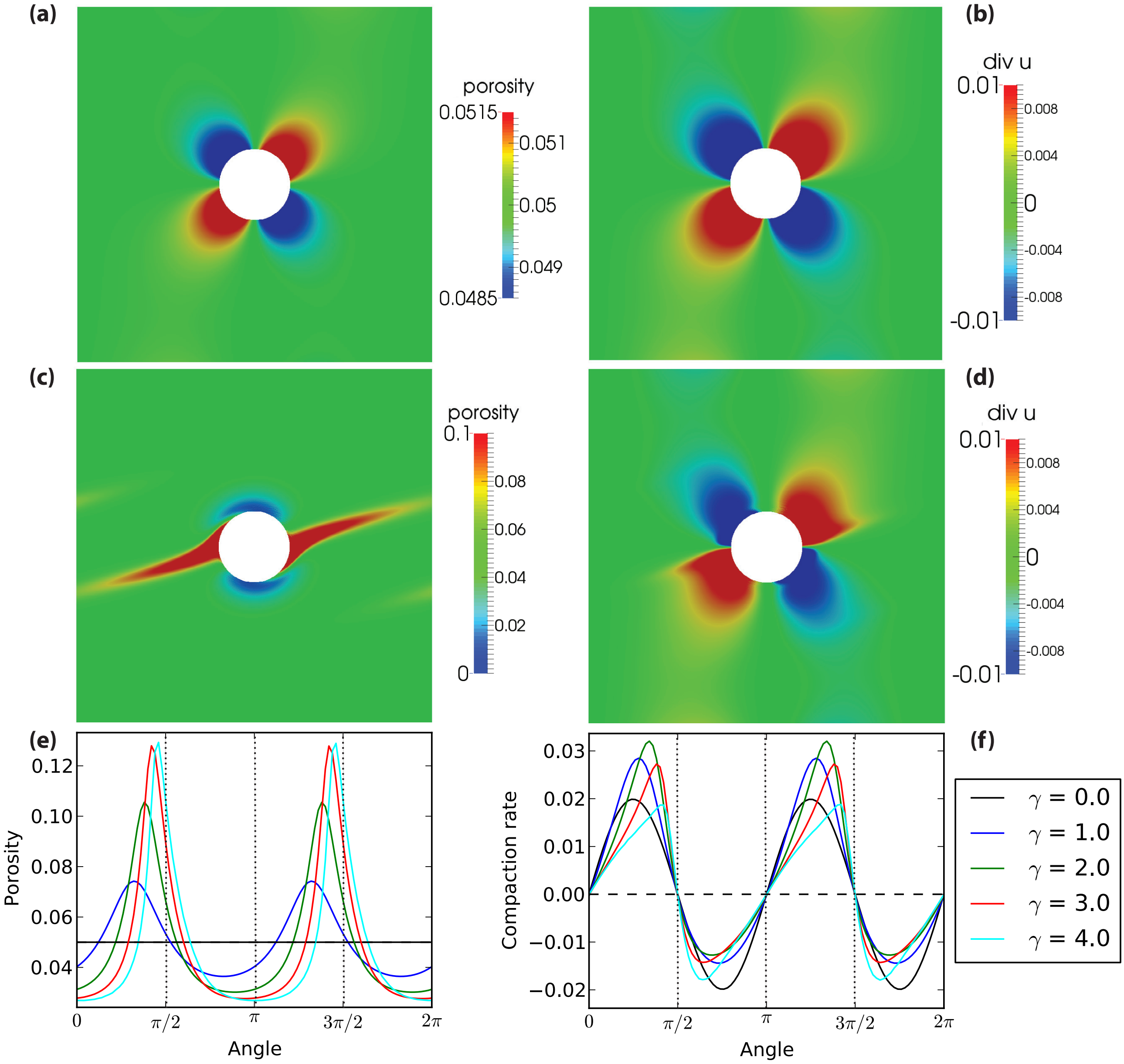

Figure 6. Porosity (left) and compaction rate (right) for a simulation with uniform initial porosity, $R = 50$ and $\alpha = 0$, at strains 0.1 (a-b) and 4.0 (c-d). (e) Porosity and (f) compaction rate integrated between a and $2a$ for different angles at various strains.

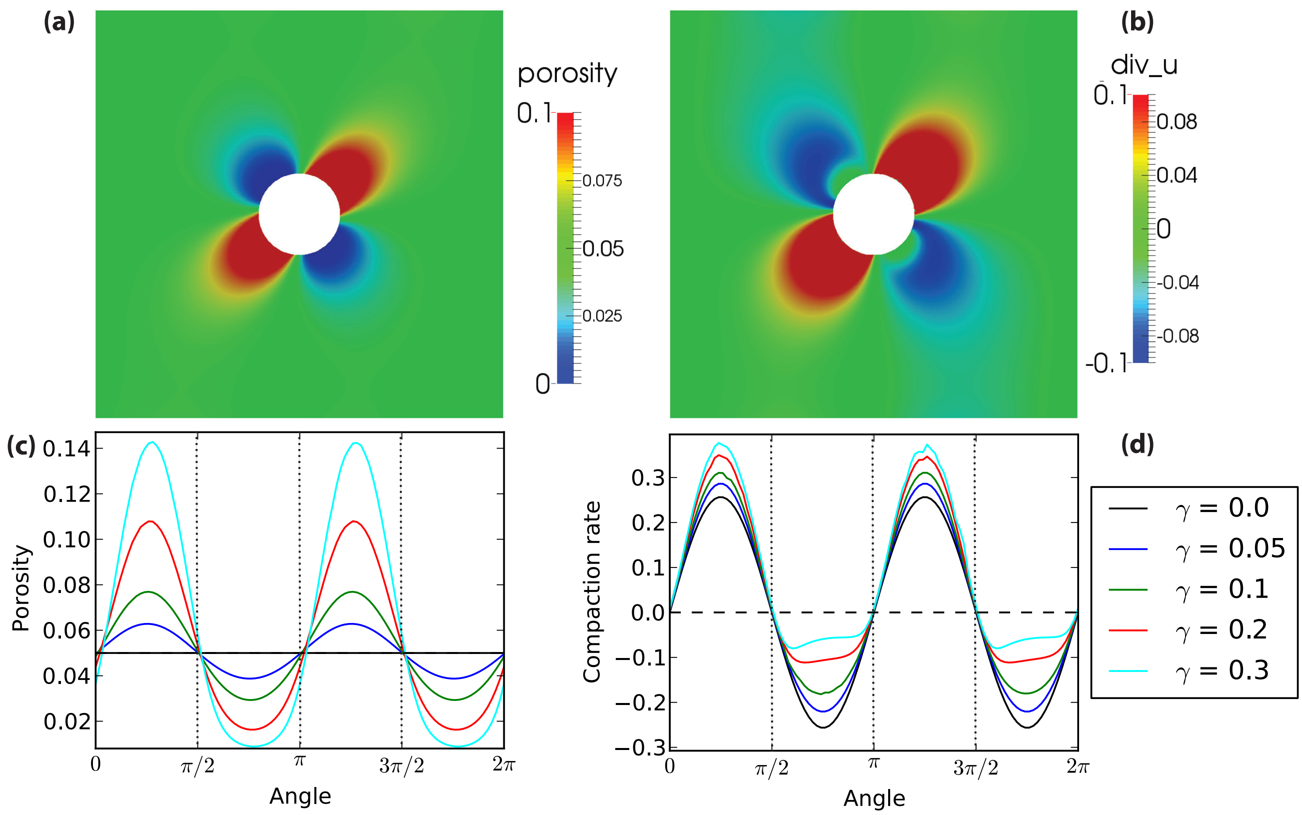

Figure 7. (a) Porosity and (b) compaction rate for a simulation with uniform initial porosity, $R = 1.7$ and $\alpha = 0$, at a strain of 0.3. (c) Porosity and (d) compaction rate integrals at various strains.

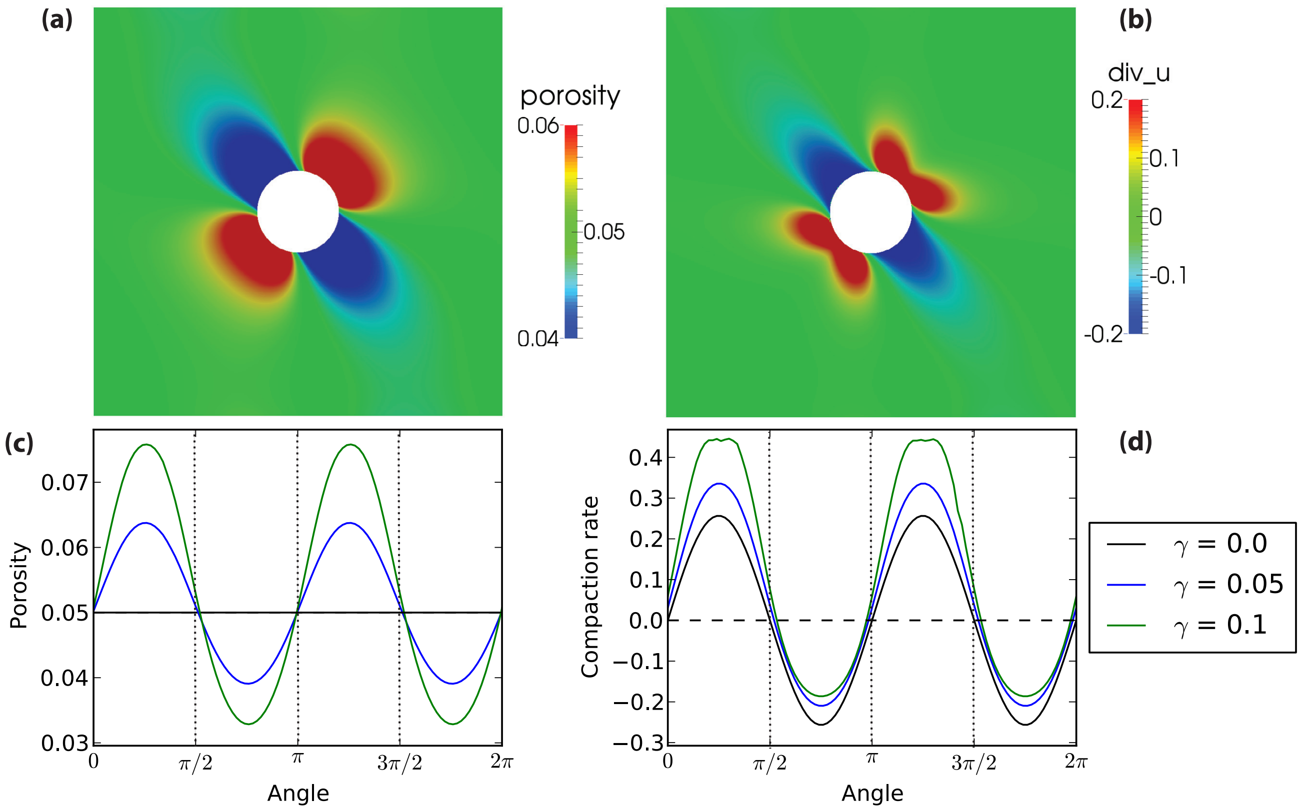

Figure 8. (a) Porosity and (b) compaction rate for a simulation with uniform initial porosity, $R = 1.7$ and $\alpha = 28$, at a strain of 0.1. (c) Porosity and (d) compaction rate integrals for various strains.

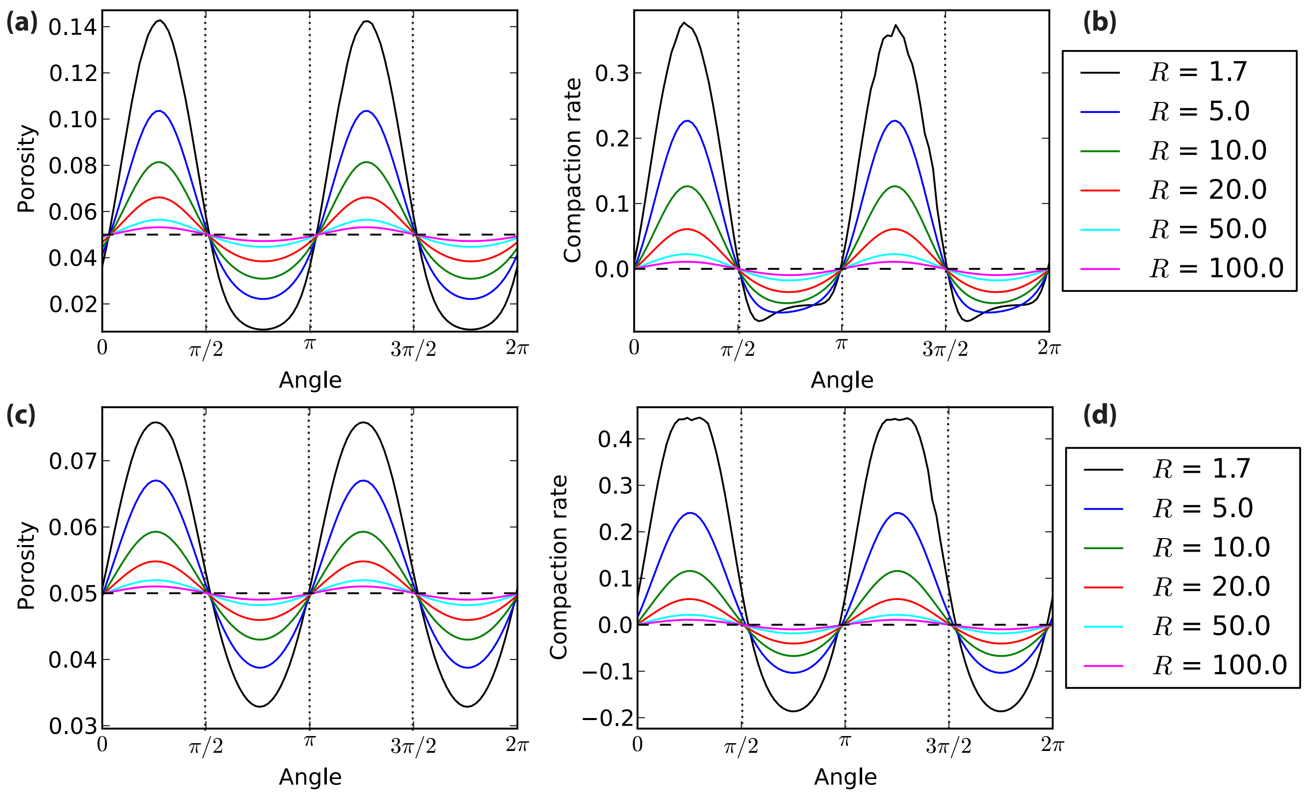

Figure 9. (a) Porosity and (b) compaction rate integrals for simulations with uniform initial porosity, $\alpha = 0$ at $\gamma = 0.3$, for various values of R. (c) Porosity and (d) compaction rate for simulations with $\alpha = 28$ at $\gamma = 0.1$, for various values of R.

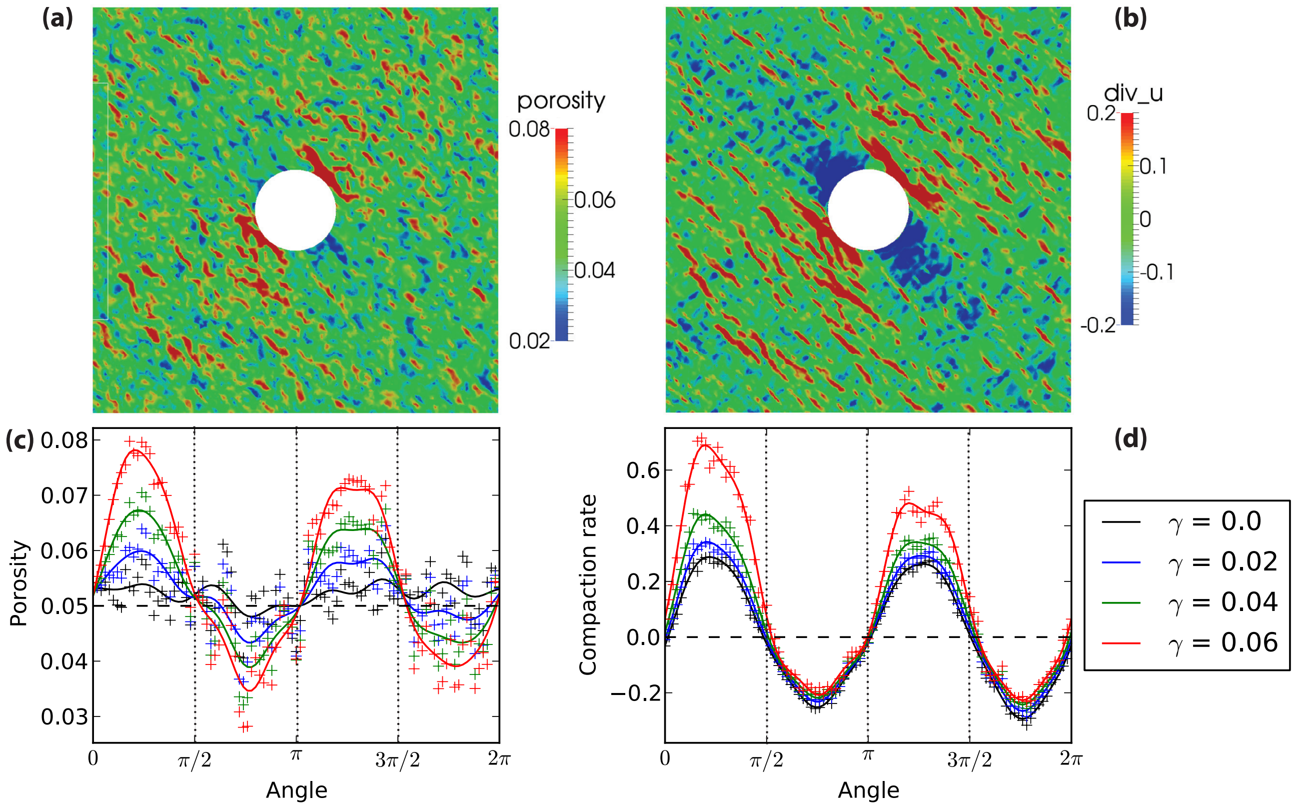

Figure 10. (a) Porosity and (b) compaction rate for a simulation with random initial porosity, $R = 1.7$ and $\alpha = 28$, at a strain of 0.06. (c) Porosity and (d) compaction rate integrals for the same simulation, at various strains. The solid lines are fits with Fourier functions with the lowest 9 coefficients included.

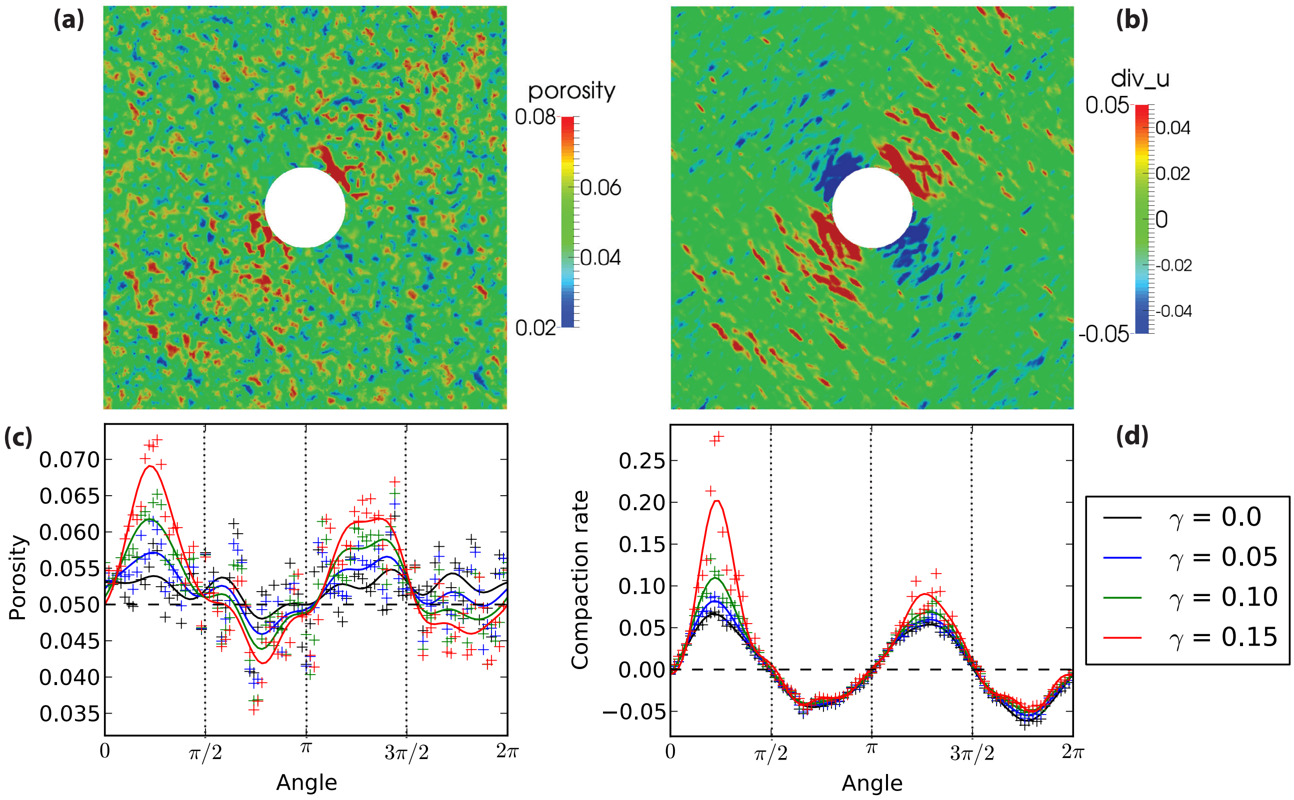

Figure 11. (a) Porosity and (b) compaction rate for a simulation with random initial porosity, $R = 20$ and $\alpha = 28$, at a strain of 0.15. (c) Porosity and (d) compaction rate integrals for the same simulation, at various strains. The solid lines are fits with Fourier functions with the lowest 9 coefficients included.

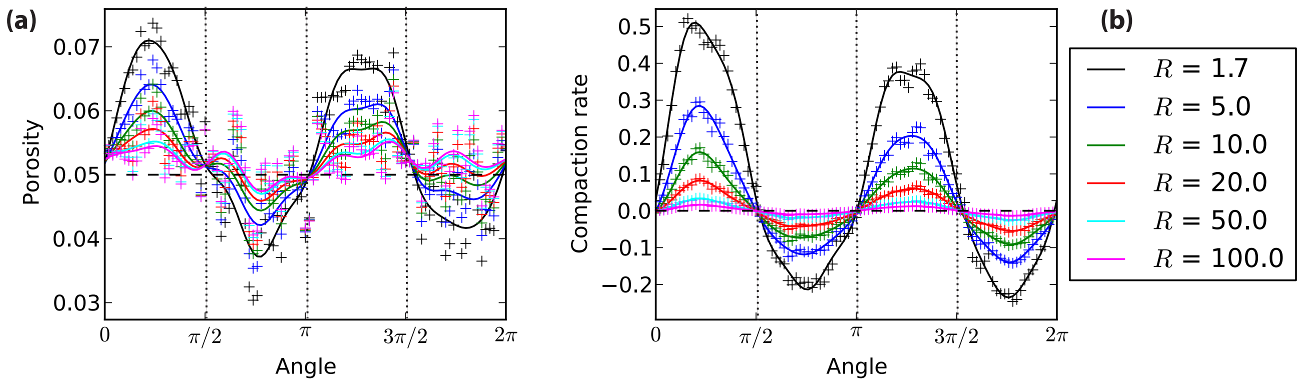

Figure 12. (a) Porosity and (b) compaction rate integrals for simulations with random initial porosity, $\alpha = 28$ at $\gamma = 0.05$, for various values of R. The solid lines are fits with Fourier functions with the lowest 9 coefficients included.

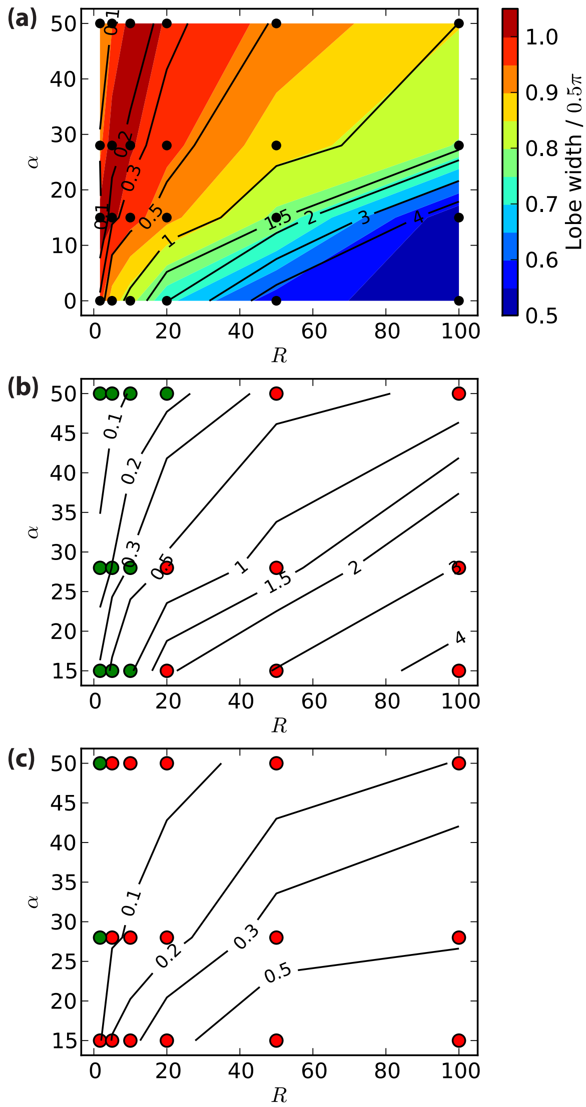

Figure 13. (a) Maximum strain $\gamma_{\max}$ reached as function of α and R (black contours) in simulations with uniform initial porosity and an inclusion. The background color denotes the scaled average width of high-porosity lobes W. The black circles indicate parameter combinations used in simulations. (b) Maximum strains in simulations with random initial porosity without an inclusion. The red circles indicate simulations that do not display significant melt bands at the final strain $\gamma_{\max}$, the green circles indicate simulations that do. (c) Maximum strains reached in simulations with random initial porosity with an inclusion.